bromide and 4.2 g (172 mmol) of magnesium turning in diethyl ether (75 mL) was added 13.9855 g (70.2 mmol) of trimethylchlorostannane. The mixture was refluxed for 3 h and hydrolyzed with saturated ammonium chloride solution and then diluted with ether (78 mL). The organic layer was separated, washed with water, (3 × 75 mL), and dried over $MgSO_4$. The organic solvent was evaporated under reduced pressure to give 11.60 g (80%) of *n*-propyltrimethylstannane: ^1H NMR (CCl_4) δ 0.04 (s, 9 H, $^2J(^{119}Sn-C-H)$ = 51.5 Hz, Sn*Me*), 1.02–0.79 (t, 3 H, SnCCCH_3).

Preparation of *tert*-Butyl-*n*-propyldimethylstannane. In a 100-mL three-necked round-bottom flask equipped with a stirrer was placed 4.50 g (21.8 mmol) of *n*-propyltrimethylstannane in 15 mL of hexane. The reaction flask was cooled to −78 °C under nitrogen. To this was added 10.9 mL of a 2.0 M solution of *tert*-butyllithium (21.8 mmol) in pentane, followed by dropwise addition of THF (10 mL). The reaction mixture was analyzed by GLPC, and after 40 min most of the organotin was consumed to yield a single product. The resulting mixture was hydrolyzed with saturated ammonium chloride solution and diluted with hexane (50 mL). The organic layer was separated and washed with water (3 × 50 mL) and then dried over $MgSO_4$. Hexane was evaporated under reduced pressure; the product *tert*-butyl-*n*-propyldimethylstannane was collected and shown to be identical by NMR spectrum with an authentic sample: ^1H NMR (CCl_4) δ −0.03 (s, 6 H, $^2J(^{119}Sn-C-H)$ = 46.5 Hz, SnMe), 1.06 (s, 9 H, $^3J(Sn-C-C-H)$ = 62.5 Hz, SnCC(CH_3)−). Anal. Calcd for $C_9H_{22}Sn$: C, 43.42; H, 8.9. Found: C, 43.52; H, 8.97.

Neohexyltrimethylstannane (5) from THF and *tert*-Butyllithium Reaction Products. Into a 100-mL flask under an atmosphere of nitrogen was placed 1.78 g (24.7 mmol) of THF. The flask was cooled to 0 °C, and 12.3 mL of 2.0 M solution of *tert*-butyllithium (24.7 mmol) in pentane was added slowly. After 1 h at 0 °C 2.2 g (12.3 mmol) of tetramethylstannane was added. GLPC analysis of a sample of the reaction mixture showed the formation of *tert*-butyltrimethylstannane (1) and neohexyltrimethylstannane (5). Compound 5 was collected from GLPC and assigned as follows: ^1H NMR (CCl_4) δ 0.03 (s, 9 H, $^2J(^{119}Sn-CH_3)$ = 51.0 Hz, SnCH_3), δ 0.83 (s, 9 H, SnCCCCH_3), 1.52–0.52 (t, 4 H, SnCH_2CH_2]. Anal. Calcd for $SnC_9H_{22}Sn$: C, 43.42; H, 8.9. Found: C, 44.23; H, 9.13.

Reaction of *tert*-Butyllithium with Tetramethylstannane in Diethyl Ether. Into a 100-mL flask was placed 1.40 g of tetramethylstannane in 3 mL of hexane. The flask was cooled to 0 °C under nitrogen. To this was added 11.7 mL of 2.0 M solution of *tert*-butyllithium (23.4 mmol) in pentane, followed by dropwise addition of diethyl ether (5 mL). The flask was warmed to room temperature. After 1 h GLPC analysis of the mixture showed the formation of *tert*-butyltrimethylstannane (1). After 24 h the reaction mixture was hydrolyzed with saturated ammonium chloride solution and diluted with 25 mL of hexane. The organic layer was separated, washed with water (3 × 25 mL), dried, and concentrated under reduced pressure. GLPC analysis of the residue showed the formation of three products: *tert*-butyltrimethylstannane (1), neohexyltrimethylstannane (5), and dineohexyldimethylstannane (6). Compounds 5 and 6 were collected from GLPC and characterized. Compound 5: ^1H NMR (CCl_4) δ 0.033 (s, 9 H, $^2J(Sn-C-H)$ = 51.0 Hz, SnCH_3), 0.83 (s, 9 H, SnCCCCH_3). Anal. Calcd for $C_9H_{22}Sn$: C, 43.42; H, 8.9. Found: C, 43.56; H, 8.9. Compound 6: ^1H NMR (CCl_4) δ 0.0 (s, 6 H, $^2J(Sn-C-H)$ = 48 Hz, SnCH_3), 0.82 (s, 18 H, SnCCC(CH_3)$_2$CH). Anal. Calcd for $C_{14}H_{32}Sn$: C, 52.69; H, 10.11. Found: C, 52.87; H, 9.96.

Acknowledgment. We are grateful for support of this work by the National Science Foundation (Grant CHE8318205) and to the donors of the Petroleum Research Fund, administered by the American Chemical Society.

Registry No. 1, 3531-47-3; 2, 35569-11-0; 3, 94859-88-8; 4, 94859-89-9; 5, 94859-86-6; 6, 94859-87-7; *n*-BuSnMe$_3$, 1527-99-7; *n*-Bu$_2$SnMe$_2$, 1528-00-3; *n*-Bu$_3$SnMe, 1528-01-4; *n*-Bu$_4$Sn, 1461-25-2; *t*-Bu$_3$SnMe, 35569-12-1; *t*-Bu$_4$Sn, 83236-77-5; Me$_4$Sn, 594-27-4; *t*-BuMe$_2$SnCH$_2$Et, 94859-85-5; Me$_3$SnCH$_2$Et, 3531-45-1; Me$_3$SnCl, 1066-45-1; PhSnMe$_3$, 934-56-5; *n*-BuLi, 109-72-8; *t*-BuLi, 594-19-4; EtBr, 74-96-4; EtCH$_2$Br, 106-94-5.

The Bonding and Interconversion in a Series of $Rh_2(CO)_4(PR_2)_2$ Isomers

Sung-Kwon Kang,[1] Thomas A. Albright,*[1,3] Thomas C. Wright,[2] and Richard A. Jones[2]

Departments of Chemistry, University of Houston, Houston, Texas 77004, and The University of Texas at Austin, Austin, Texas 78712

Received August 27, 1984

Extended Hückel molecular orbital calculations were carried out on the square planar–square planar (PP), square planar–tetrahedral (PT), and tetrahedral–tetrahedral (TT) isomers of $Rh_2(CO)_4(PH_2)_2$ which serves as a model for a series of bridging phosphido transition-metal dimers. After geometrical optimization the relative energies of the three isomers are quite close to each other at this computational level: PP, 0, PT, 4, and TT, 7 kcal/mol. Interconversion of the PP isomer with the PT form is symmetry forbidden when a C_2 axis is maintained along the rotational itinerary. Relaxation of this symmetry constraint by hinging the $Rh(CO)_2$ units along the rotation path makes the reaction symmetry allowed. The activation energy is tremendously lowered by this hinging distortion, from 56 to 23 kcal/mol. The activation energy for the direct conversion of the PT isomer to the TT one was 9 kcal/mol, and this path was found to be symmetry allowed for a least-motion pathway. A number of reaction paths from PP to TT have been found to be symmetry forbidden and hence energetically inaccessible. The bonding in each structure is discussed with particular attention to the Rh–Rh interaction and unequal Rh–P bond lengths. Finally, the optimal structures of the reduced anion and dianion of $Rh_2(CO)_4(PH_2)_2$ were determined. A comparison is made to the electrochemical behavior of known complexes.

Introduction

There has been a recent surge of interest in the preparation and categorization of phosphido-bridged transition-metal complexes.[4,5] This is partly due to the fact that the PR_2 unit is a stable and highly flexible bridging ligand;

(1) University of Houston.
(2) The University of Texas at Austin.
(3) Camille and Henry Dreyfus Teacher-Scholar, 1980–1984. Alfred P. Sloan Research Fellow, 1982–1986.

(4) For reviews see: (a) Carty, A. J. *Adv. Chem. Ser.* **1982**, *No. 196*, 163; *Pure Appl. Chem.* **1982**, *54*, 113. (b) Vahrenkamp, H. *Angew. Chem., Int. Ed. Engl.* **1978**, *17*, 379. (c) Robinson, S. D. *MTP Int. Rev. Sci., Part 2* **1976**, *6*, 133. (d) Hayter, R. G. *Prep. Inorg. React.* **1965**, *2*, 211.

0276-7333/85/2304-0666$01.50/0

consequently it tolerates a wide variety of metals and unusual bonding situations. To our knowledge there has been only three prior theoretical studies on bridging phosphido complexes.[6,7]

Our attention was initially drawn to a series of $Rh_2L_4(PR_2)_2$ compounds which have been structurally determined[8] where L is a neutral, two-electron donor ligand. These dimers exist, in the solid state, in one of three isomeric forms. They are most easily identified by the local coordination geometry around each rhodium atom as square planar–square planar (PP), square planar–tetrahedral (PT), or tetrahedral–tetrahedral (TT). Three closely related examples are provided by **1–3**.[8a,b] Electron counting predicts a net Rh–Rh bond order of 0, 1, and 2 for **1–3**, respectively. The Rh–Rh distances follow this

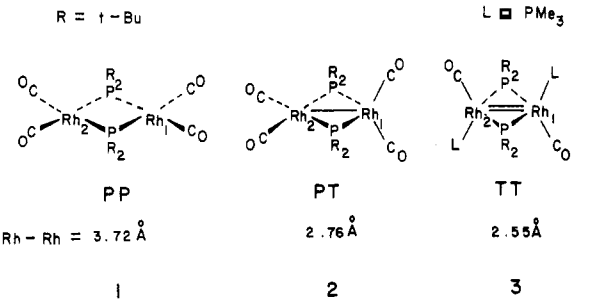

prediction nicely. The Rh–Rh distance of 2.76 Å in **2** falls within the range of distances (2.62–2.84 Å) observed for other rhodium dimers where a single bond is thought to exist.[9] Two electron reduction of **2** (or **1**) yields a tetrahedral–tetrahedral complex, **4**, which formally contains a

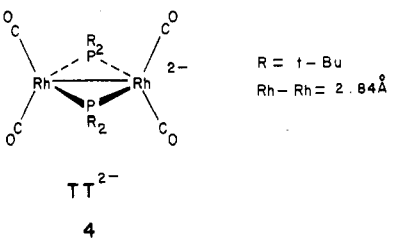

Rh–Rh single bond.[8b] The second point to note is that the energy difference between **1** and **2** must be very small. Normally mixtures of **1** (PP) and **2** (PT) are formed when $[Rh(CO)_2(t\text{-}Bu_2P)]_2$ is crystallized from hexane solutions.[8a] Rapid cooling to −35 °C produces only the PP isomer, whereas slow cooling to −35 °C affords the PT isomer. No crystalline samples of the neutral TT isomer have been obtained for this compound under a variety of conditions; however, two closely related analogs have been found to have this geometry.[8b,c] Therefore, it is reasonable to expect that the TT isomer is also energetically close to the PP and PT forms. We are not aware of any other examples in the literature where two or three isomers of a compound, differing in metal–metal bond order, can coexist.

^{13}C NMR spectroscopy studies[8a,10] of $[Rh(CO)_2(t\text{-}Bu_2P)]_2$ show that this compound exhibits interesting dynamic behavior in solution. The carbonyl region of a ^{13}CO-enriched sample at −85 °C is consistent only with a PT formulation. Two sets of carbonyl resonances are observed, each are coupled to ^{103}Rh and ^{31}P nuclei in the expected manner. Therefore, the ground-state structure for this compound in solution is PT. Upon warming the sample the two resonances broaden and coalesce, and at +50 °C a sharp doublet of triplets is observed. The high-temperature spectrum is compatible with either a static structure of D_{2h} symmetry (PP or TT geometries) or a dynamic one with the PT isomer rapidly interconverting with PP and/or TT. We prefer the latter interpretation based on the spectral behavior at intermediate temperatures and the high-temperature values of the ^{103}Rh–^{13}C and ^{31}P–^{13}C coupling constants.

This manuscript reports the results of molecular orbital calculations at the extended Hückel[11] level on $Rh_2(CO)_4(PH_2)_2$. Computational and geometric details are given in the Appendix. We shall concentrate our attention on the electronic and geometrical requirements for interconver-

(5) For recent leading references see: (a) Jones, R. A.; Stuart, A. L.; Atwood, J. L.; Hunter, W. E. *Organometallics* **1983**, *2*, 874. (b) Jones, R. A.; Stuart, A. L.; Atwood, J. L.; Hunter, W. E.; Rogers, R. D. *Ibid.* **1982**, *1*, 1721. Jones, R. A.; Stuart, A. L.; Atwood, J. L.; Hunter, W. E. *Ibid.* **1983**, *2*, 1437. Atwood, J. L.; Hunter, W. E.; Jones, R. A.; Wright, T. C. *Inorg. Chem.* **1983**, *22*, 993. Jones, R. A.; Stuart, A. L.; Wright, T. C. *J. Am. Chem. Soc.* **1983**, *105*, 7459. Jones, R. A.; Lasch, J. G.; Norman, N. C.; Wright, T. C. *Ibid.* **1983**, *105*, 6184. Jones, R. A.; Lasch, J. G.; Norman, N. C.; Stuart, A. C.; Wright, T. C.; Whittlesey, B. R. *Organometallics* **1983**, *3*, 114. (c) Carty, A. J.; Hartstock, F.; Taylor, N. J. *Inorg. Chem.* **1982**, *21*, 1349. Carty, A. J.; MacLaughlin, S. A.; Taylor, N. J. *J. Organomet. Chem.* **1981**, *204*, C27. Mott, G. N.; Granby, R.; MacLaughlin, S. A.; Taylor, N. J.; Carty, A. J. *Organometallics* **1983**, *2*, 189. (d) Harley, A. D.; Whittle, R. R.; Geoffroy, G. L. *Ibid.* **1983**, *2*, 60. Harley, A. D.; Guskey, G. J.; Geoffroy, G. L. *Ibid.* **1983**, *2*, 53. Foley, H. C.; Finch, W. C.; Pierpont, C. G.; Geoffroy, G. L. *Ibid.* **1982**, *1*, 1379. Breen, M. J.; Schulmann, P. M.; Geoffroy, G. L.; Rheingold, A. L.; Fultz, W. C. *Ibid.* **1984**, *3*, 782. Breen, M. J.; Geoffroy, G. L. *Ibid.* **1982**, *1*, 1437. Breen, M. J.; Duttera, M. R.; Geoffroy, G. L.; Novotanak, G. C.; Roberts, D. A.; Schulman, P. M.; Steinmetz, G. R. *Ibid.* **1982**, *1*, 1008. Breen, M. J.; Geoffroy, G. L.; Rheingold, A. L. *J. Am. Chem. Soc.* **1983**, *105*, 1069. Burkhardt, E. W.; Mercer, W. C.; Geoffroy, G. L. *Inorg. Chem.* **1984**, *23*, 1779. (e) Keller, E.; Vahrenkamp, H. *Chem. Ber.* **1979**, *112*, 234. Muller, M.; Vahrenkamp, H. *Ibid.* **1983**, *116*, 2322. Vahrenkamp, H.; Wolters, D. *Organometallics* **1982**, *1*, 874. Fischer, K.; Vahrenkamp, H. *Z. Anorg. Allg. Chem.* **1981**, *475*, 109. (f) Braustein, P.; Mott, D.; Fars, O.; Louer, M.; Grandjean, D.; Fisher, J.; Mitschler, A. *J. Organomet. Chem.* **1981**, *213*, 79. Bender, R.; Braustein, P.; Metz, B.; Lemoine, P. *Organometallics* **1984**, *3*, 381. (g) Keiter, R. L.; Madigan, M. J. *Ibid.* **1982**, *1*, 409. (h) Haines, R. J.; Steen, N. D. C. T.; English, R. B. *J. Chem. Soc., Dalton Trans.* **1984**, 515. English, R. B.; Haines, R. J.; Steen, N. D. C. T. *S. Afr. J. Chem.* **1983**, *36*, 109. Haines, R. J.; Steen, N. D. C. T.; English, R. B. *Ibid.* **1983**, *36*, 130; *J. Organomet. Chem.* **1981**, *209*, C34. (i) Iwasaki, F.; Mays, M. J.; Raithby, R. R.; Taylor, P. L.; Wheatley, P. J. *Ibid.* **1981**, *213*, 185. Mays, M. J.; Raithby, P. R.; Taylor, P. L. *Ibid.* **1982**, *224*, C45. Iggo, J. A.; Mays, M. J.; Raithby, P. R.; Henrick, K. *J. Chem. Soc., Dalton Trans.* **1984**, 515. (j) Zolk, R.; Werner, H. *J. Organomet. Chem.* **1983**, *252*, C53. (k) Yu, Y.-F.; Gallucci, J.; Wojcicki, A. *J. Am. Chem. Soc.* **1983**, *105*, 4826. Yu, Y.-F.; Chau, C.-N.; Wojcicki, A.; Calligaris, M.; Nardin, G.; Balducci, G. *Ibid.* **1984**, *106*, 3704. (l) Young, D. A. *Inorg. Chem.* **1981**, *20*, 2049. (m) Schumann, H.; Heisler, M. *Chem. Ber.* **1979**, *112*, 541. Schumann, H.; Neumann, L. *Z. Naturforsch., B: Anorg. Chem., Org. Chem.* **1981**, *36B*, 708. (n) Schäfer, H. *Ibid.* **1979**, *34B*, 1358. (o) Nobile, C. F.; Vasapollo, G.; Giannoccaro, P.; Sacco, A. *Inorg. Chim. Acta* **1981**, *48*, 261. (p) Meek, D. W.; Waid, R.; Tau, K. D.; Kirchner, R. M.; Morimoto, C. N. *Ibid.* **1982**, *64*, L221.

(6) (a) Burdett, J. K. *J. Chem. Soc., Dalton Trans.* **1977**, 423. (b) Teo, B. K.; Hall, M. B.; Fenske, R. F.; Dahl, L. F. *Inorg. Chem.* **1975**, *14*, 3103.

(7) Summerville, R. H.; Hoffmann, R. *J. Am. Chem. Soc.* **1976**, *98*, 7240.

(8) (a) Jones, R. A.; Wright, T. C.; Atwood, J. L.; Hunter, W. E. *Organometallics* **1983**, *2*, 470. (b) Jones, R. A.; Wright, T. C. *Ibid.* **1983**, *2*, 1842. (c) Jones, R. A.; Norman, N. C.; Seeberger, M. H.; Atwood, J. L.; Hunter, W.E. *Ibid.* **1983**, *2*, 1629. (d) Gaudiello, J. G.; Wright, T. C.; Jones, R. A.; Bard, A. J., Submitted for publication. (e) Jones, R. A.; Wright, T. C.; Atwood, J. L.; Hunter, W. E., unpublished information. (f) Kreter, P. E.; Meek, D. W. *Inorg. Chem.* **1983**, *22*, 319. (g) Meek, D. W.; Kreter, P. E.; Christoph, G. G. *J. Organomet. Chem.* **1982**, *231*, C53. (h) Fultz, W. C.; Rheingold, A. L.; Kreter, P. E.; Meek, D. W. *Inorg. Chem.* **1983**, *22*, 860. (i) See also: Kreter, P. E.; Meek, D. W.; Christoph, G. G. *J. Organomet. Chem.* **1980**, *188*, C27. Jamerson, J. D.; Pruett, R. L.; Billing, E.; Fiato, F. A. *Ibid.* **1980**, *193*, C43. Billig, E.; Jamerson, J. D.; Pruett, R. L. *Ibid.* **1980**, 192, C49. Haines, R. J.; Steen, N. D.; English, R. B. *Ibid.* **1981**, *209*, C34.

(9) See, for example: Cowie, M. *Inorg. Chem.* **1979**, *18*, 286. Cowie, M.; Dwight, S. K. *Ibid.* **1980**, *19*, 209 and references therein.

(10) Jones, R. A., unpublished information.

(11) Hoffmann, R. *J. Chem. Phys.* **1963**, *39*, 1397. Hoffmann, R.; Lipscomb, W. N. *Ibid.* **1962**, *36*, 2179; **1962**, *37*, 2872.

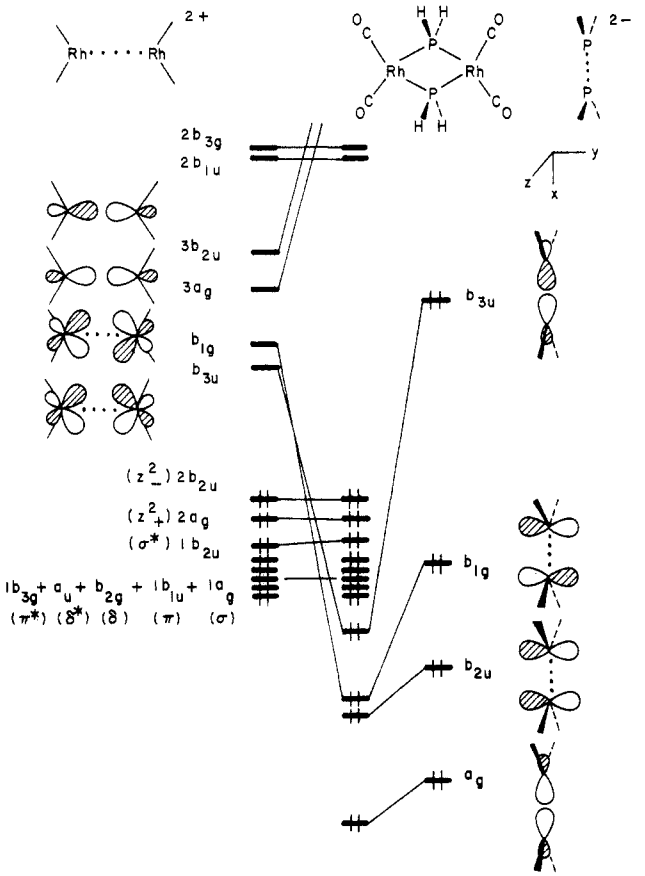

Figure 1. An orbital interaction diagram for the PP isomer.

sion between the isomers along with the bonding in the PT structure. But before we do so, it is necessary to develop the electronic structure in the PP and TT isomers.

The Square Planar–Square Planar and Tetrahedral–Tetrahedral Geometries

The electronic structures of PP and TT $Rh_2(CO)_4(PH_2)_2$ has been briefly discussed by Summerville and Hoffmann[7] in the context of a large series of $M_2L_4X_2$ dimers. The analysis used here follows a slightly different approach. The important valence orbitals of the PP isomer can easily be constructed by interacting a $Rh_2(CO)_4^{2+}$ unit, **5**, with the bridging $(PH_2)_2^{2-}$ species, **6**. Each PH_2^- unit has two

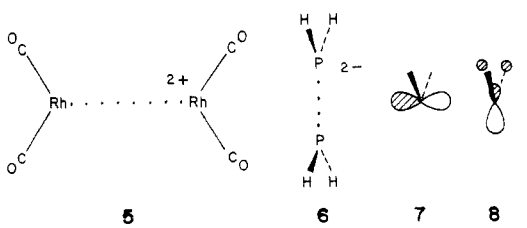

5 **6** **7** **8**

important valence orbitals; a p orbital localized on phosphorus, **7**, and a hybrid orbital directed away from the hydrogens, **8**. Both orbitals are filled using the electron counting scheme that we have adopted. Linear combinations of **7** and **8** are then taken to construct the four valence orbitals of $(PH_2)_2^{2-}$. These are shown on the right side of Figure 1. In a similar fashion the valence orbitals of the $Rh_2(CO)_4^{2+}$ fragment are constructed from the in-phase and out-of-phase combinations of the seven orbitals of $Rh(CO)_2^+$ which are shown in **9**. The orbitals of a C_{2v} ML_2 fragment have been developed elsewhere.[12] It is more

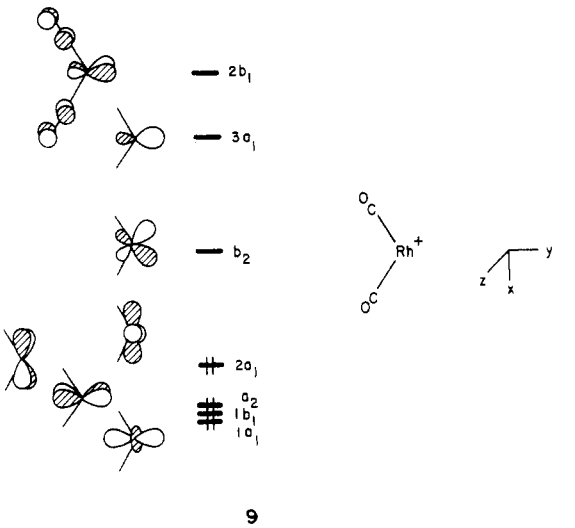

9

convenient to use the unconventional coordinate shown in **9** to express these orbitals. At low energy is a block of four d-centered levels. They have y^2, yz, xz, and $z^2 - x^2$ character. The b_2 orbital is primarily xy with some metal x character so that it is hybridized out away from and antibonding to the carbonyl σ functions. At higher energies the $3a_1$ orbital is a primarily metal s and y combination. Finally, the high-lying $2b_1$ level is mainly metal z bonding to carbonyl π^*. Metal yz also mixes into this orbital in an antibonding fashion to carbonyl π^*.

Since the Rh–Rh distance in the PP isomer is very long (3.72 Å in **1**), the linear combinations of two $Rh(CO)_2^+$ units will not be split apart much in energy. This is reflected in the ordering of the levels for $Rh_2(CO)_4^{2+}$ on the left side of Figure 1. The orbitals for both fragments have been labeled in this figure to conform to the D_{2h} symmetry in the molecule. The b_{2u} and a_g combinations of $(PH_2)_2^{2-}$ are stabilized primarily by the $3b_{2u}$ and $3a_g$ fragment orbitals, respectively, in $Rh_2(CO)_4^{2+}$. The remaining two occupied levels in $(PH_2)_2^{2-}$, b_{1g} and b_{3u}, interact very strongly with empty b_{1g} and b_{3u} in $Rh_2(CO)_4^{2+}$. Therefore, four low-lying, occupied molecular orbitals form the Rh–P bonds in the dimer. Four empty levels corresponding to the antibonding interaction between these fragment orbitals are also formed. They lie at very high energies and are not shown in Figure 1. Left behind are eight filled orbitals which do not interact much with the bridging phosphido groups. The labels in parentheses for them in Figure 1 refer to the familiar metal–metal interaction mode. When the two $Rh(CO)_2^+$ fragments are combined, there is some intermixing between the $1a_1$ and $2a_1$ (see **9**) orbitals. The σ and σ^* levels ($1a_g$ and $1b_{2u}$, respectively) have $x^2 - y^2$ character. The $2a_g$ and $2b_{2u}$ molecular orbitals are the in-phase and out-of-phase combinations of metal z^2 (z_+^2 and z_-^2, respectively). It is clear from this description of the electronic structure in the PP isomer that no direct Rh–Rh bond is present; nor is any expected from the long Rh–Rh distance in, for example, **1**. Note that the two lowest unoccupied molecular orbitals are predicted to be the π and π^* combinations of the metal p orbitals ($2b_1$ in **9**). They will figure into our discussion when we examine how the PP isomer interconverts with the PT and TT structures.

(12) (a) Burdett, J. K. *Inorg. Chem.* **1975**, *14*, 375; *J. Chem. Soc., Faraday Trans. 2* **1974**, *70*, 1599. (b) Elian, M.; Hoffmann, R. *Inorg. Chem.* **1975**, *14*, 1058. (c) Mingos, D. M. P. *J. Chem. Soc., Dalton Trans.* **1977**, 602; *Adv. Organomet. Chem.* **1977**, *15*, 1. (d) Hofmann, P. *Angew. Chem.* **1977**, *89*, 551. (e) Albright, T. A.; Hoffmann, R.; Thibeault, J. C.; Thorn, D. L. *J. Am. Chem. Soc.* **1979**, *101*, 3801. Albright, T. A. *Tetrahedron* **1982**, *38*, 1339.

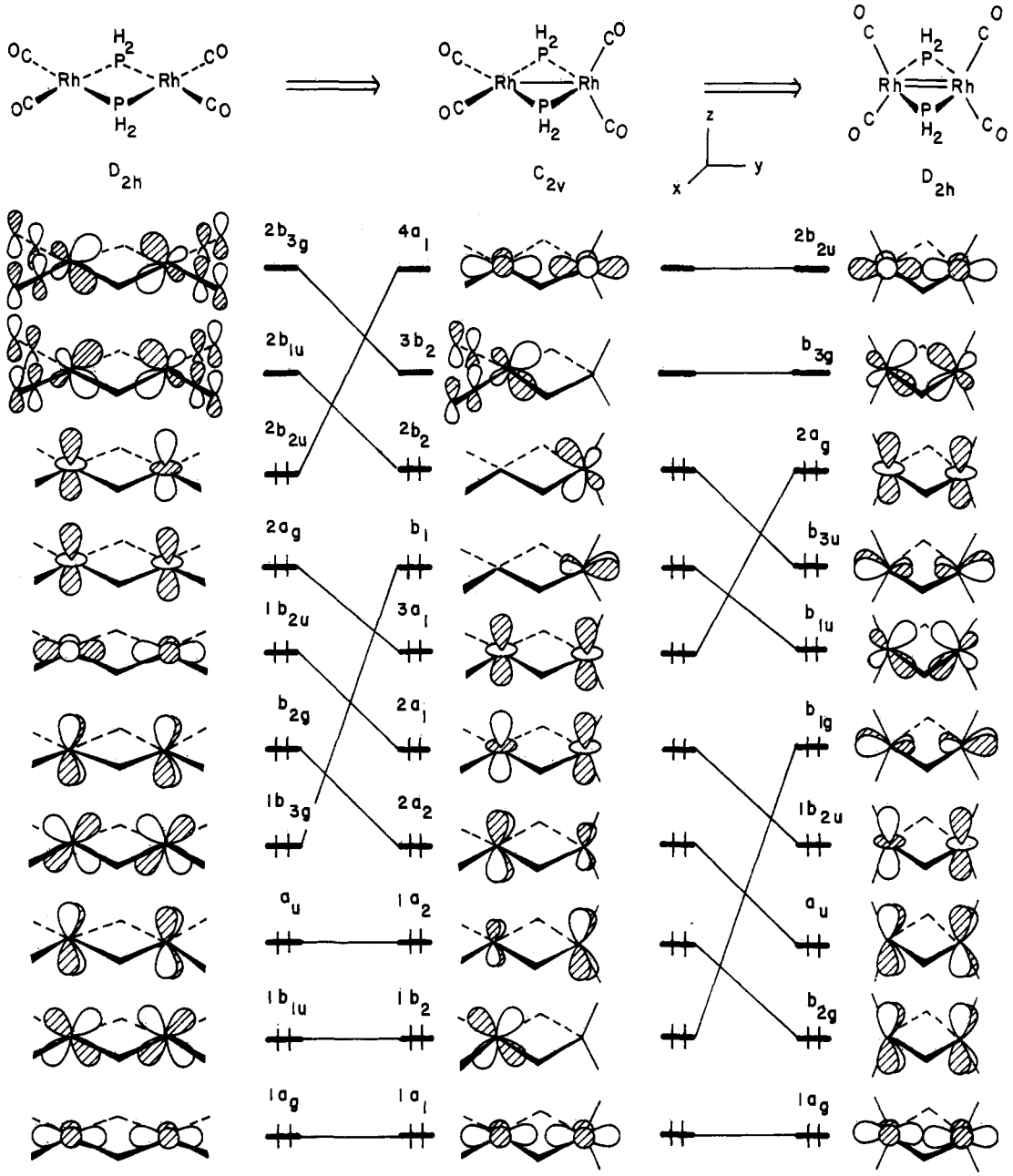

Figure 2. The relationship of the molecular orbitals in the PP, PT, and TT structures. The levels are arranged in order of energy but are not quantitative.

There is an easier way to derive the orbital structure than the fragment approach in Figure 1. The resultant, metal-centered molecular orbitals of the PP isomer are displayed on the left side of Figure 2. Examination of the form of these orbitals and their relative energies in Figure 1 leads one to the realization that the orbital structure is nothing more than the bonding and antibonding combinations of a square-planar splitting pattern, **10**. Thus, the

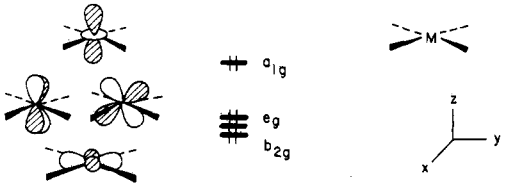

10

two highest occupied orbitals for a d^8–d^8 dimer are derived from z^2 (a_{1g}). Below these are the six occupied levels which originate from xz, yz, and $x^2 - y^2$ ($e_g + b_{2g}$). Their energetic ordering follows the normal sequence $\sigma < \pi < \delta < \delta^* < \pi^* < \sigma^*$; however, a small splitting is observed due to the long Rh–Rh distance.

The orbital structure for the TT geometry in $Rh_2(CO)_4(PH_2)_2$ can be derived in an analogous fashion. There is one important difference which must be taken into account. The Rh–Rh distance decreases from 3.72 to 2.55 Å in the TT isomer. Consequently the direct Rh–Rh interaction becomes much larger. An interaction diagram for the $Rh_2(CO)_4^{2+}$ fragment is presented in Figure 3. The δ-type orbitals derived from a_2 and $2a_1$ in each $Rh(CO)_2^+$ unit are still not split to any great extent. There are three sets of π orbitals, originating from $1b_1$, b_2, and $2b_1$. The combinations from $2b_1$ ($2b_{1g}$ and $2b_{3u}$) are not separated much in energy. Recall that a substantial amount of density in $2b_1$ is centered on the carbonyl π^* functions, thus the overlap between the $2b_1$ orbitals is reduced. The larger splitting in the b_2 set compared to $1b_1$ is due to the

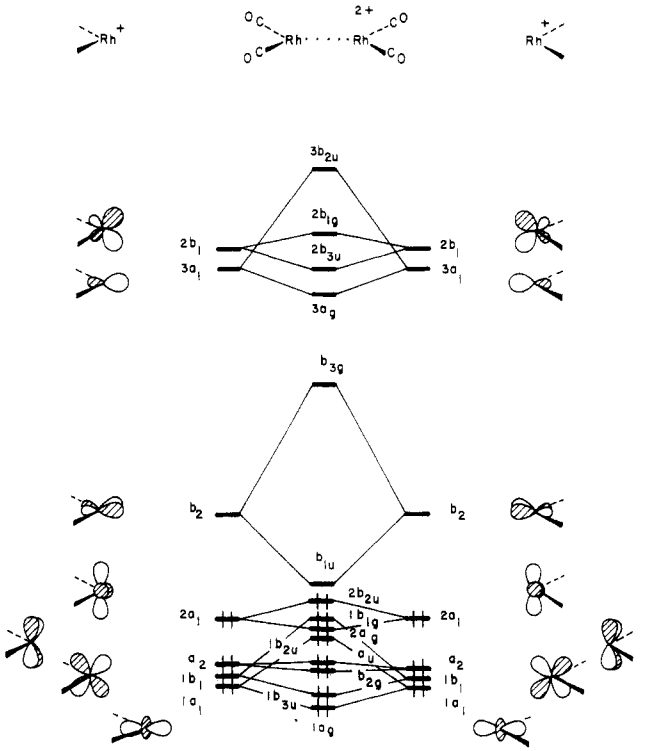

Figure 3. An interaction diagram for the construction of the orbitals in the $Rh_2(CO)_4^{2+}$ fragment at the TT geometry.

hybridization in the former. Finally, notice that the σ^* level, derived from the antibonding combination of $1a_1$ functions, stays at low energy in the $Rh_2(CO)_4^{2+}$ fragment. This is due to the mixing of $3a_1$ character into this orbital. When the PH_2^- units are taken into account, there will be a considerable remixing between the $1b_{2u}$ and $2b_{2u}$ levels.

Figure 4 shows the important interactions between the $Rh_2(CO)_4^{2+}$ and $(PH_2)_2^{2-}$ fragments. The P–P distance in 1 of 1.47 Å increases to 1.95 Å in **3**. Therefore, the splitting of **7** and **8** on the right side of Figure 4 is not as large as it was in the PP isomer. There are also, unfortunately, more complicating features in the interaction diagram for the TT complex. Once again the filled a_g and b_{2u} orbitals of $(PH_2)_2^{2-}$ are stabilized predominantly by the metal sp hybrids $3a_g$ and $3b_{2u}$. The b_{1g} fragment orbital of $(PH_2)_2^{2-}$ interacts strongly with $1b_{1g}$ and $2b_{1g}$ on $Rh_2(CO)_4^{2+}$. Three molecular orbitals are formed. The lowest MO is concentrated on the phosphido bridges. Metal xy and x mix into it in a bonding way so that the functions at each metal are hybridized toward the phosphido groups. The middle level, labeled b_{1g} in Figure 4, is basically nonbonding and is concentrated on the two Rh atoms. Here the $Rh_2(CO)_4^{2+}$ $1b_{1g}$ and $2b_{1g}$ fragment orbitals are mixed in an antibonding and bonding fashion, respectively, with the b_{1g} level of $(PH_2)_2^{2-}$. At very high energy and not shown in Figure 4 is the fully antibonding combination between the three b_{1g} fragment orbitals. An identical three-orbital pattern emerges for the interaction between b_{3u} on $(PH_2)_2^{2-}$ and the $1b_{3u}$, $2b_{3u}$ set from $Rh_2(CO)_4^{2+}$. In both cases the bonding and nonbonding molecular orbitals are filled. The $\delta(b_{2g})$, $\delta^*(a_u)$, $\pi(b_{1u})$, and $\pi^*(b_{3g})$ levels of $Rh_2(CO)_4^{2+}$ are basically unperturbed by the bridging phosphido ligands. There is considerable intermixing between the $1a_g$ and $2a_g$ along the $1b_{2u}$ and $2b_{2u}$ orbitals on $Rh_2(CO)_4^{2+}$ as a result of overlap with the a_g and b_{2u} set from $(PH_2)_2^{2-}$. The orbital construction can be determined by application of second-order perturbation theory; however, we shall only quote the result here. The molecular orbital labeled $1a_g$ becomes a Rh–Rh σ-bonding orbital while $2b_{2u}$ is rehybridized into a high-lying σ^* MO. The $1b_{2u}$, $2a_g$ set evolve into the out-of-phase and in-phase combinations of x^2 (using the coordinate system at the top of Figure 4).

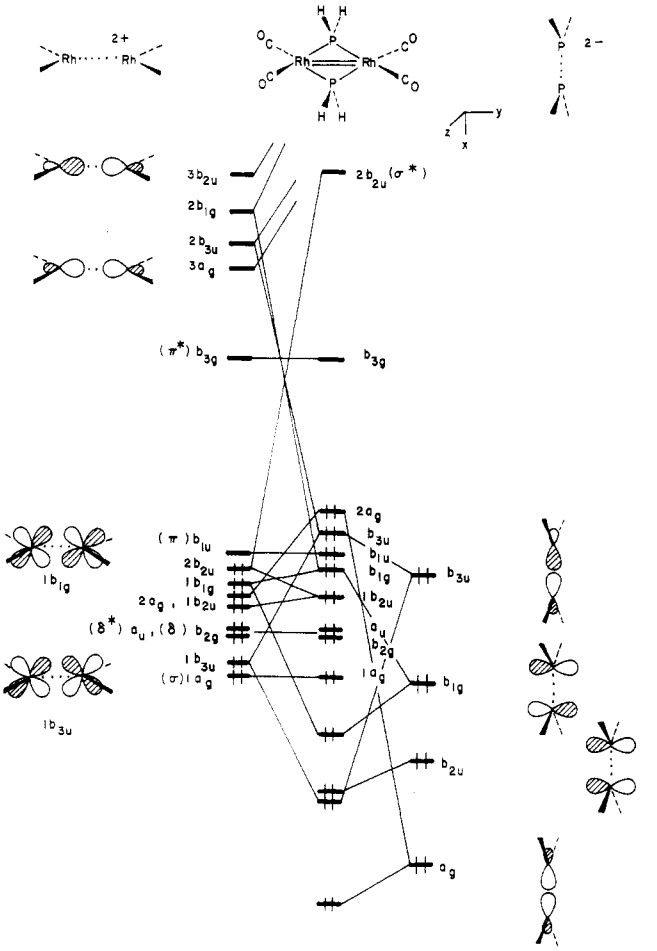

Figure 4. An orbital interaction diagram for the TT isomer of $Rh_2(CO)_4(PH_2)_2$.

The resultant metal-centered molecular orbitals for the TT isomer are redrawn on the far right side of Figure 2. Plots of the σ, π, π^*, and σ^* orbitals are displayed in Figure 5. Notice that the π and π^* orbitals are contained within the plane defined by the $Rh_2(CO)_4$ portion of the molecule. All four orbitals contain appreciable density on the carbonyls. This is especially evident for the π^* and σ^* molecular orbitals which have a heavy involvement of carbonyl π^*. The σ orbital also has carbonyl π^* mixed into it while the π orbital contains mainly carbonyl σ. We are well aware of the difficulties in assigning metal–metal bond orders when bridging ligands are present.[13] However, with $\sigma + \pi$ filled and $\sigma^* + \pi^*$ empty it seems clear that the Rh–Rh bond order is two. This is consistent with the very short Rh–Rh bond observed for **3**.

Referring back to the molecular orbitals of the TT isomer in Figure 2, one can also see the emergence of two superimposed blocks of tetrahedrally based molecular orbitals. The splitting pattern for a tetrahedron is shown in **11** using a coordinate system consistent with that in Figure 4. For convenient reference the L′ ligands in **11** can be considered to be bridging phosphido groups. The $x^2 - y^2$ component of the e set forms the σ ($1a_g$) and σ^* ($2b_{2u}$) molecular orbitals of the dimer. Likewise, the yz member of the t_2 set forms the π (b_{1u}) and π^* (b_{3g}) orbitals. Ap-

(13) Benard, M.; Dedieu, A.; Nakamura, S. *Nouv. J. Chim.* **1984**, *8*, 149. Bernard, M. *J. Am. Chem. Soc.* **1978**, *100*, 7740; *Inorg. Chem.* **1979**, *18*, 2782 and references therein.

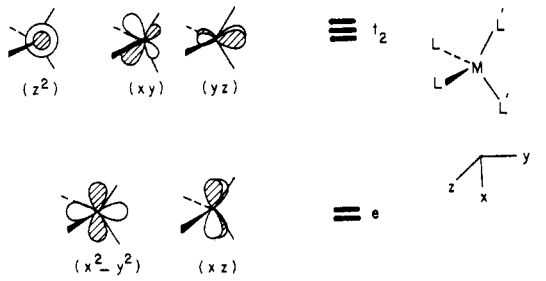

11

preciable through-space interaction exists for each combination, and consequently they are split in energy to a large extent. The remaining three orbitals at each tetrahedral center do not overlap much with each other. One should be cautioned, however, that the bonding combinations of the z^2 and xy tetrahedral orbitals lie at *higher* energies than their antibonding counterparts (see Figure 2). This is due to through-bond interactions[14] with the bridging phosphido units. In each case the bonding combination forms a sizable overlap with and is destabilized by a $(PH_2)_2^{2-}$ combination.

The Square Planar–Tetrahedral Isomer and the Dynamics of Interconversion

We are now at a position to describe the interconversion of the PP isomer to the TT one. A reasonable path would be to proceed via the PT geometry. A Walsh diagram that displays only the metal-centered valence orbitals is given in Figure 6. Here the rotational angles θ_1 and θ_2 are defined as the dihedral angle formed between each Rh-$(CO)_2$ unit and the xy plane, as shown in **12**. On the left

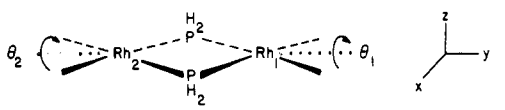

12

half of Figure 6, θ_1 is varied and θ_2 is held constant so PP is converted into the PT isomer. An important proviso is that this is a rigid rotation; Rh_2, it's carbonyl groups and the phosphido groups remain in the xy plane, and furthermore, Rh_2 and associated carbonyls retain planarity along the rotational path. The Rh–Rh bond distance was uniformly decreased from 3.72 to 2.76 Å (as in **2**). The Rh–P bond lengths were held constant, thus the P–Rh–P bond angles open as θ_1 increases. The filled molecular orbitals derived from $1b_{1u}$, a_u, b_{2g}, and $2a_g$ along with the empty $2b_{3g}$ stay at constant energy as θ_1 increases from 0° to 90°. The reader should refer back to Figure 2 for the explicit form of these molecular orbitals and their correlated products at the PT geometry. The σ level, $1a_g$, is stabilized since the Rh–Rh distance decreases as θ_1 increases. For the same reason one would expect that π^*, $1b_{2u}$, should rise to be very high energy. Instead it undergoes a strongly avoided crossing with $2b_{2u}$, and it is this level which rises to high energy. Both orbitals intermix with each other so that $2b_{2u}$ ultimately becomes a σ^* orbital in the PT isomer. It is labeled $4a_1$ in Figures 2 and 6. The π^* orbital, $1b_{3g}$, also rises to appreciably high energy during rotation. The component at Rh_1 moves into the xy plane and is destabilized by a phosphido lone-pair combination. A high-lying empty molecular orbital formed from the antibonding combination of b_{3u} on $Rh_2(CO)_4^{2+}$ and b_{3u} of $(PH_2)_2^{2-}$, **13**, will also be stabilized greatly on rotation.

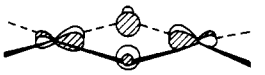

13

Antibonding between metal d at Rh_1 and the phosphido functions are lost. However, this level undergoes a strongly avoided crossing with $2b_{1u}$. The latter orbital is stabilized and becomes $2b_2$ in Figures 2 and 6.

We have presented a rather simplified discussion of the first half of the Walsh diagram in Figure 6. This is a least-motion process for rotation which maintains C_2 symmetry. A goodly number of other intermixings occur between molecular orbitals in this reduced symmetry. The resultant orbital of the PT isomer tend to localize on either the square-planar or tetrahedral rhodium atoms with the important exception of σ ($1a_1$) and σ^* ($4a_1$). This localization can be traced to other avoided crossings. The orbital structure of the PT isomer can be derived either by a detailed inspection of the Walsh diagram or by interaction of a D_{2d} $Rh_2(CO)_4^{2+}$ fragment with $(PH_2)_2^{2-}$. Neither method is very informative. Inspection of the resultant molecular levels at the middle of Figure 2, however, shows that they are the linear combinations of the square-planar and tetrahedral splitting patterns (see **10** and **11**). The only combination with sufficient overlap at this distance to cause a large splitting occurs between b_{2g} on the square-planar end with the $x^2 - y^2$ component of the e set at the tetrahedron. This forms the σ and σ^* bonds. Plots of these two orbitals are presented in Figure 7. It is again apparent that carbonyl π^* mixes into each molecular orbital. Notice also that there is approximately equal density on each rhodium atom; i.e., the σ bond appears to be covalent.

Returning back to the Walsh diagram in Figure 6, the important point is that this least-motion "reaction" is symmetry forbidden. Filled $2b_{2u}$ on the PP side of the reaction becomes the empty σ^* ($4a_1$) at PT. Likewise, empty $2b_{1u}$ is stabilized until it becomes the filled $2b_2$ level. At any intermediate geometry the symmetry of these orbitals is a and b, respectively, so they can and will cross. A plot of the relative energies vs. rotation for the least-motion path is shown by the dashed line in Figure 8a. The orbital crossing engenders a very high activation energy; we calculate it to be 56 kcal/mol. The crossing point occurs at $\theta_1 = 51°$. The computed Rh–Rh overlap population also behaves in an interesting manner as θ_1 increases and the Rh–Rh distance decreases. This is shown by the dashed line in Figure 8b. Its initial value at the PP geometry is small and negative (–0.066). This is consistent with no net Rh–Rh bonding. As the rotation proceeds the overlap population becomes more negative. At the crossing point there is a hysteresis; the Rh–Rh overlap population suddenly increases since σ^* at this point becomes empty and the overlap population rises to a value of 0.131 at the PT geometry. Finally, notice in Figure 8a that within the constraints that we have chosen for this reaction path, the PT structure is 16 kcal/mol *less* stable than PP. This is anticipated by the Walsh diagram in Figure 6. The $2b_2$ HOMO in the PT isomer is clearly at higher energy than the $2b_{2u}$ HOMO at the PP geometry. Furthermore, the rise in energy of $1b_{3g}$ to the b_1 level is only partly compensated for the lowering of $1a_g$ to $1a_1$.

Clearly the high activation energy for this path and its endothermic nature is at variance to the experimental results which were discussed in the Introduction. Relaxation of the geometrical constraints that we have imposed on this reaction alters this situation markedly. Three

(14) Hoffmann, R. *Acc. Chem. Res.* **1971**, *4*, 1.

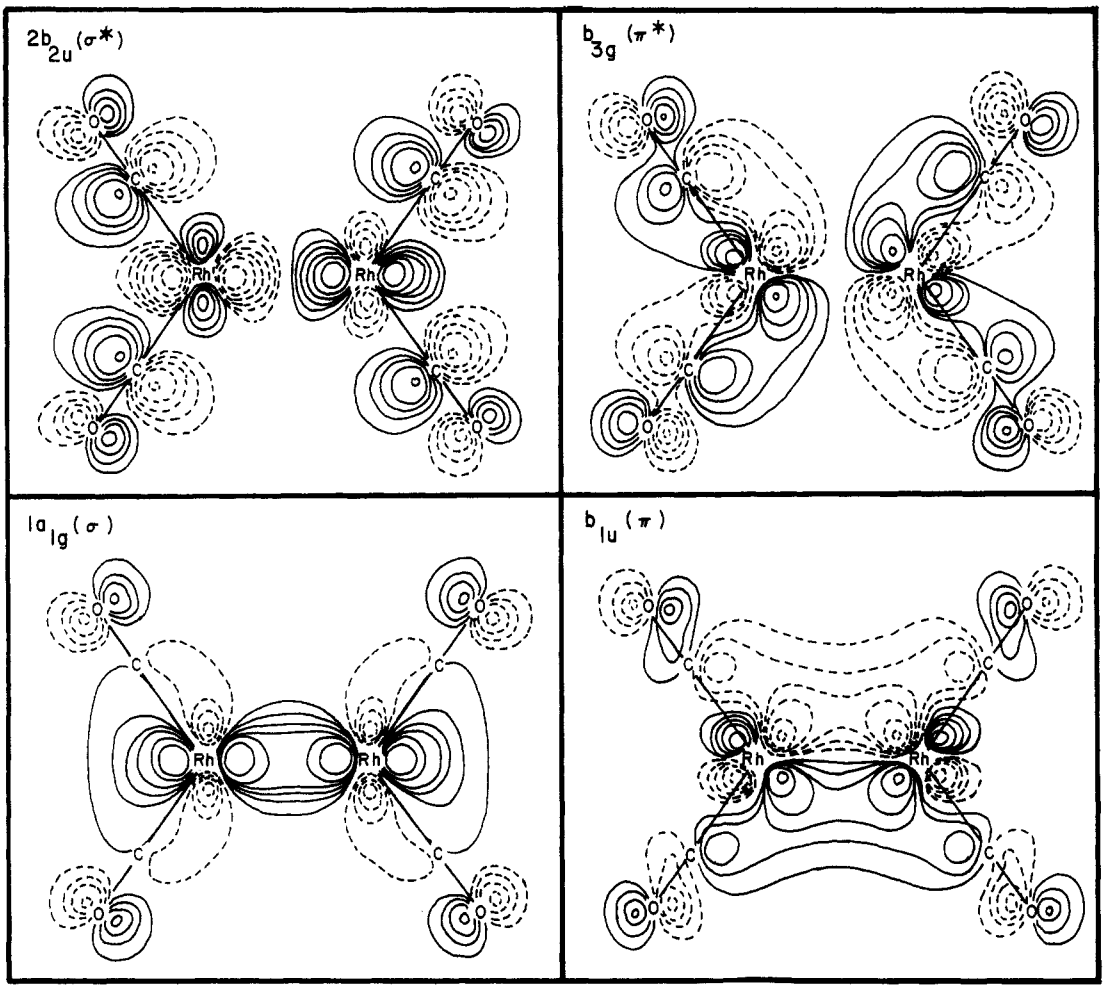

Figure 5. Contour plots of the σ, π, π^*, and σ^* orbitals in the TT isomer of $Rh_2(CO)_4(PH_2)_2$. Values of the plotted wave function are ±0.025, ±0.05, ±0.075, ±0.10, ±0.15, ±0.20, and ±0.40. Solid and dashed lines represent positive and negative values, respectively, of the wave function. The orbitals have been plotted so that the $Rh_2(CO)_4$ unit lies in the plane of the paper and consequently the two PH_2 groups (not shown) lie in the front and back of this plane.

additional degrees of freedom were optimized along the reaction path. Both $Rh(CO)_2$ groups were allowed to hinge by varying λ_1 and λ_2, as shown in **14**. Here λ_1 and λ_2 are

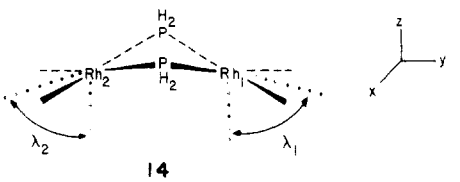

14

defined as the angle made between the $Rh(CO)_2$ planes and the z axis. The Rh–Rh along with the Rh–P distances were also independently optimized. In the PP isomer we find optimium Rh–Rh and Rh–P distances of 3.76 and 2.51 Å, respectively. This compares favorably with **1** where the Rh–Rh distance is 3.72 Å and the Rh–P distances average to 2.38 Å. There is an extremely flat potential for hinging in $Rh_2(CO)_4(PH_2)_2$. An optimized value of $\lambda_1 = \lambda_2 = 84°$ was found. In **1**[8a] as well as a structure[8e] where R = CH_2CMe_3 the values of λ_1 and λ_2 were 90°. This structure is only 0.3 kcal/mol higher in energy than our optimized structure. Furthermore, in the closely related $Rh_2(DPPE)_2(PPh_2)_2$ molecule λ_1 and λ_2 are 76.7°.[8h] In our calculations this is only 0.7 kcal/mol above the ground state. Summerville and Hoffmann[7] have discussed this hinging motion in the context of several d^8 square-planar-bridged dimers including the phosphido system. We agree with their assessment that no one single orbital is responsible for controlling the distortion. What is critical in our study is that hinging during the rotation breaks the symmetry from C_2 to C_1. The HOMO and LUMO on the left side of the Walsh diagram in Figure 6 now have the same symmetry so they will never cross but rather undergo an avoided crossing with each other. We computed a transition state for the rotation process at $\theta_1 = 60°$, $\lambda_1 = 80°$, and $\lambda_2 = 50°$. In other words, the rhodium atom which remains square planar (Rh_2 in **14**) hinges more at the transition state than it does at the PP geometry. At the transition state the HOMO–LUMO gap is 0.65 eV. The Rh_1–P distances were 2.24 Å and those for Rh_2–P were 2.53 Å. As shown by the solid line in Figure 8a, the energy of the transition state is lowered dramatically to 23.3 kcal/mol. The Rh–Rh overlap population given by the solid line in Figure 8b now smoothly increases along the reaction path. At the PT geometry we find no tendency to hinge. The Rh–Rh bond length optimized at 2.76 Å which is identical with that observed in **2**.[8a] In $(Et_3P)_2Rh(\mu\text{-}PPh_2)_2Rh(COD)$[8g] which is also at the PT geometry the Rh–Rh distance was found to be 2.75 Å. In this structure as well as in **2** the Rh–P bond lengths are markedly asymmetric. We compute them to be Rh_1–P = 2.24 Å and Rh_2–P = 2.46 Å. They are in excellent agreement with those observed for **2** (2.10 and 2.46 Å, respectively). This asymmetry causes the PT structure to become stabilized greatly. It now lies only 4 kcal/mol higher in energy than the PP isomer.

The longer Rh–P bonds to the square-planar vs. tetrahedral center has an electronic origin. When we do a

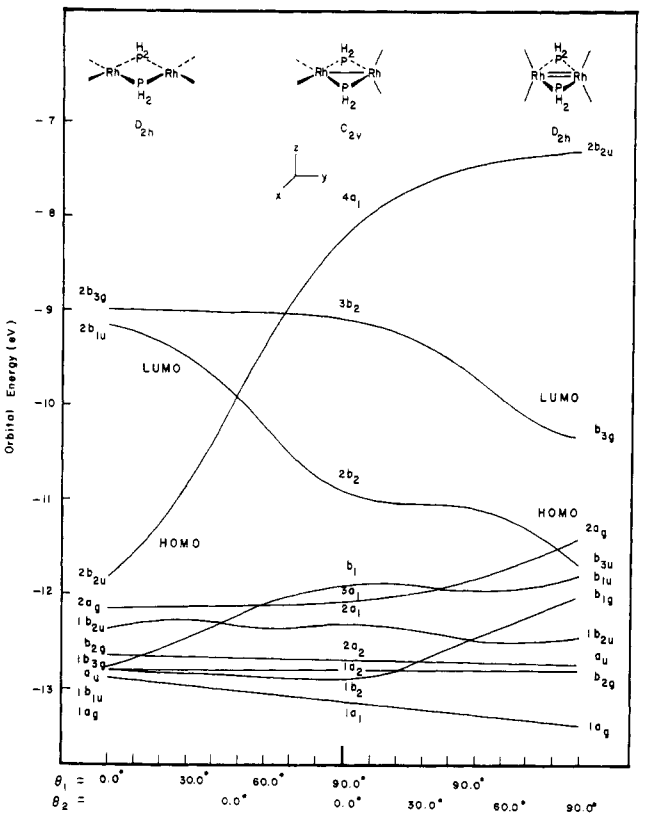

Figure 6. A Walsh diagram for rotation (increasing θ_1 and θ_2 as defined in **12**) in $Rh_2(CO)_4(PH_2)_2$.

calculation on the PT isomer where the phosphido groups bridge symmetrically at an averaged Rh–P distance, the Rh_1-P overlap population is 0.598 and that for Rh_2–P is 0.476. This has nothing to do with any Rh–Rh interaction. A computation on **15a** and **15b** yields Rh–P overlap pop-

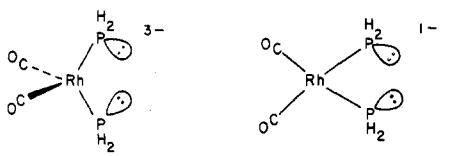

15a **15b**

ulations of 0.473 and 0.388, respectively. In this particular case the difference in overlap populations can be readily explained. At Rh_1 in the PT isomer as well as **15a** the local environment is an 18-electron tetrahedral one. All three Rh 5p atomic orbitals are utilized in bonding to the surrounding ligands. At Rh_2 (and **15b**) there is a local 16-electron square-planar coordination. Now only two Rh 5p atomic orbitals are used in ligand bonding. The remaining 5p atomic orbital effectively remains empty and nonbonding (the $3b_2$ molecular orbital in Figure 2). Therefore, the Rh–P bonding to the 18-electron, tetrahedral side is stronger than that to the 16-electron, square-planar end. The Rh–P overlap population difference can be traced in this manner to a few molecular orbitals which we shall not do here. But we caution the reader that this effect is not universal. Metal–ligand bond lengths in tetrahedral complexes are more commonly longer than those for square-planar analogues.[15] In fact, in **16** the Ni_1–P distances average to 2.23 Å while the Ni_2–P ones are 2.16 Å.[5a] The

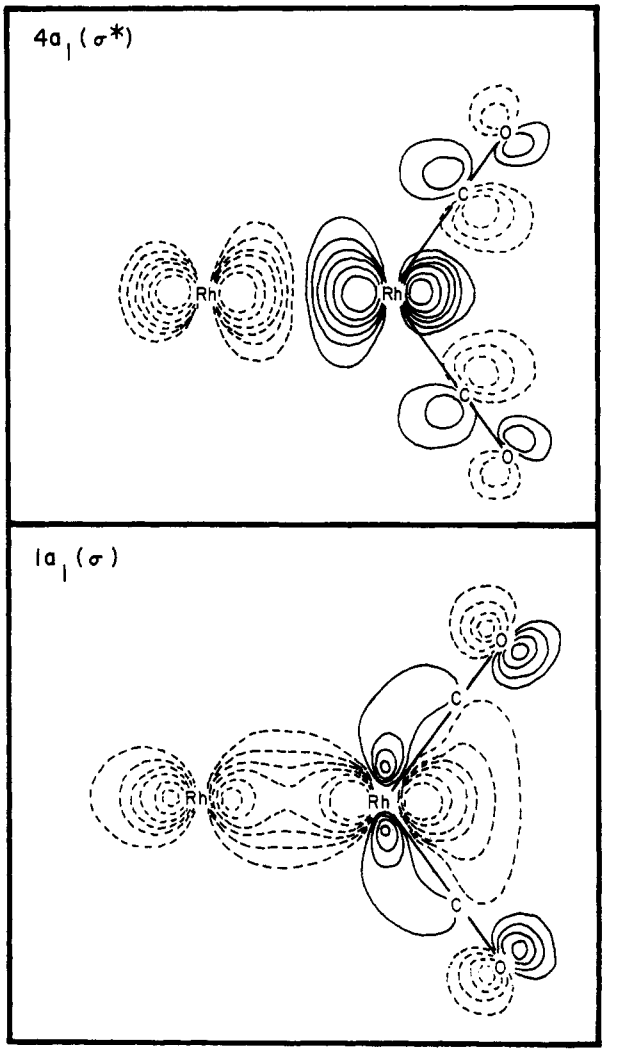

Figure 7. Contour plots of the σ and σ^* orbitals in the PT isomer. The carbonyl groups for the Rh atom on the left side of the molecule (the square-planar end) along with the bridging phosphido groups lie on either side of the plane of the paper and are not shown. Values of the contours are given in Figure 5.

rationale behind these counterexamples will be given elsewhere.[16]

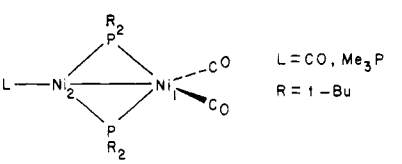

16

Returning back to the Walsh diagram in Figure 6, we shall now discuss the conversion from the PT isomer to TT. Increasing θ_2 (see **12**) from 0° to 90° smoothly transforms the orbitals of PT to those of TT. There is no HOMO–LUMO crossing. The $2b_2$ HOMO at the PT geometry correlates to occupied b_{3u}. Likewise the $3b_2$ LUMO becomes the unoccupied π^* (b_{3g}) level at the TT geometry. Notice that $3b_2$ is stabilized as θ_2 increases. This result may seem counterintuitive since π^* is clearly Rh–Rh antibonding while $3b_2$ is localized on one rhodium atom. Recall, however, that the $3b_2$ orbital is primarily derived from a Rh 5p atomic orbital. The π^* level at the TT

(15) Muir, K. W. "Molecular Structure by Diffraction Methods"; The Chemical Society: London, 1973; Vol. 1, p 580.

(16) (a) Albright, T. A.; Burdett, J. K.; Whangbo, M.-H. "Orbital Interactions in Chemistry"; Wiley: New York, 1985. (b) Kang, S.-K., to be submitted for publication.

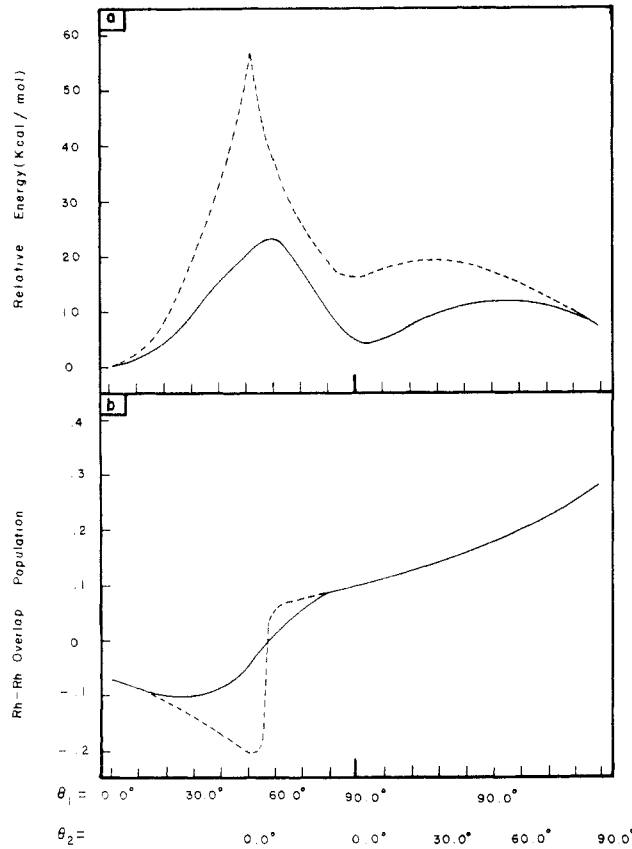

Figure 8. (a) Plots of the relative total energy of $Rh_2(CO)_4(PH_2)_2$ vs. rotation angles, θ_1 and θ_2. (b) Variation of the Rh–Rh overlap population. In each graph the dashed line refers to the least-motion path for rotation and the solid line represents that derived from the optimized reaction path.

geometry is mainly a Rh 4d orbital (see Figure 5). The increasing contribution of metal d character causes $3b_2$ to be stabilized along the reaction path. $1b_2$, b_1, $2b_2$, and $3b_2$ undergo a complicated pattern of avoided crossings to produce the π and π^* orbitals (along with b_{1g} and b_{3u}). The production of an occupied π orbital in the TT isomer causes the Rh–Rh overlap population to increase (Figure 8b) to a value of 0.319. Finally, there are two occupied levels, $1b_2$ and $3a_1$, in the PT isomer which appreciably rise in energy as θ_2 increases. In both cases repulsion from the phosphido groups is increased upon rotation. It is for this reason that the TT isomer is computed to be somewhat less stable than the PP and PT forms. At the fully optimized level TT is 7 kcal/mol less stable that PP. The optimized Rh–Rh and Rh–P distances were 2.42 and 2.24 Å, respectively. The agreement with the structure of 3[8b] is fair. In 3 the Rh–Rh and Rh–P distances were 2.55 and 2.33 Å, respectively. Figure 8a shows that full optimization does not change much the activation energy for the PT to TT conversion. A transition state at $\theta_2 = 54°$ ($\lambda_1 = \lambda_2 = 90°$) with Rh–Rh, Rh_1–P, and Rh_2–P distances of 2.65, 2.17, and 2.40 Å, respectively, were found. The activation energy was found to be 8 kcal/mol relative to the energy of the PT isomer.

There are two alternative paths that can be considered for the direct interconversion of the PP and TT isomers. Simultaneous rotation of both $Rh(CO)_2$ units in the same direction, as shown in **17**, maintains C_{2h} symmetry along the reaction path. This has been examined by Summerville and Hoffmann[7] for d^8–d^8 halide-bridged dimers. Although there are minor differences in the level ordering for what we have given for the phosphido-bridged dimers, the outcome of this reaction path is the same. The $2b_{2u}$

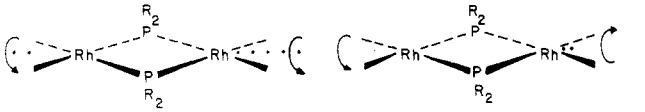

17 18

HOMO (at PP, see Figure 6) will have b_u symmetry along the reaction path. At some point it must cross the $2b_{1u}$ LUMO which has a_u symmetry. Puckering the $Rh(CO)_2$ units does not remove the symmetry-forbidden nature of this reaction. The reaction path maintains C_s symmetry, thus $2b_{2u}$ becomes a′ while $2b_{1u}$ is a″. Rotation of the $Rh(CO)_2$ units in an opposite sense, as shown in **18**, does not help matters. Now D_2 symmetry is conserved. The $2b_{2u}$ HOMO is b_2 while the $2b_{1u}$ LUMO has b_1 symmetry; the reaction remains forbidden. Puckering the $Rh(CO)_2$ groups lowers the symmetry to C_2, but the HOMO and LUMO still have different symmetries and consequently will cross. Therefore, all likely paths for the conversion of the PP isomer to the TT one are symmetry forbidden and a high reaction barrier is engendered (analogous to the least-motion path for the PP to PT rotation).

In summary, we find that the PP isomer is 4 kcal/mol more stable than the optimized PT structure. This is not in agreement with the results for **1** and as discussed in the Introduction. This may well be due to the approximate nature of the extended Hückel method. However, it is also reasonable to presume that the bulky *tert*-butyl groups on the phosphido ligands in **1** and **2** will have a larger steric interaction with the carbonyl ligands in a square-planar environment than that encountered at a tetrahedral geometry. This should destabilized **1** relative to **2** (and TT). The TT isomer is the least stable structure from our calculations which employ sterically nondemanding ligands. It lies 7 kcal/mol above PP. The available experimental work[5,8] on d^8–d^8 $M_2L_4(PR_2)_2$ complexes suggests that a TT geometry is found to be the ground state only when at least one auxillary ligand at each metal is more sterically demanding than CO. A distinctly non-least-motion path interconverts PP and PT with an associated activation energy of 23 kcal/mol (relative to PP). The PT isomer undergoes a facile rotation to TT with an activation barrier of 8 kcal/mol (relative to PT). As discussed in the Introduction, the high-temperature NMR data for $[Rh(CO)_2(t\text{-}Bu_2P)]_2$ is consistent with rapid rotation about the Rh–Rh axis. Our calculations predict that rotation from PT to TT requires a lower activation energy than that from PT to PP, but we encourage work at a higher computational level to establish this point more firmly.

Reduced $Rh_2(CO)_4(PR_2)_2$ Complexes

The electrochemical behavior of $Rh_2(CO)_4(t\text{-}Bu_2P)_2$, **2**, has been studied in some detail.[8d] There are several unusual features that come from this work. Reduction of **2** occurs via an ECE mechanism. That is, a chemical isomerization step of PT to TT is coupled between the two one-electron reductions to yield a dianion. This is understandable by looking back at the Walsh diagram in Figure 6. The $2b_{1u}$ or $3b_2$ LUMO at PP or PT, respectively, lie a much higher energy than does π^* in the TT isomer. Our calculations put TT^- at 35 kcal/mol lower in energy than PT^-. Adding one further electron accentuates this difference; TT^{2-} is 63 kcal/mol more stable than PT^{2-}. Any one-electron computational technique like extended Hückel cannot reliably give redox potentials. However, the fact that the reduction potential for addition of the second electron is lower than that for the first, despite coulombic considerations, is in agreement with our postulate that π^* at TT lies much lower in energy than the

Table I. Parameters Used in the Extended Hückel Calculations

orbital	H_{ii}, eV	ξ_1	ξ_2	C_1[a]	C_2[a]
Rh 4d	−12.50	4.29	1.97	0.5807	0.5685
5s	−8.09	2.135			
5p	−4.57	2.10			
P 3s	−18.60	1.75			
3p	−14.00	1.30			
C 2s	−21.40	1.625			
2p	−11.40	1.625			
O 2s	−32.30	2.275			
2p	−14.80	2.275			
H 1s	−13.60	1.30			

[a] Contraction coefficients used in the double-ζ expansion.

LUMO in PT. Since π^* is doubly occupied in TT^{2-}, the formal Rh–Rh bond order is reduced to one. In our calculations the Rh–Rh overlap population drops from 0.319 in TT to 0.144 in TT^{2-} (where the Rh–Rh distance was kept identical with that in **3**). A geometric consequence of this is that the Rh–Rh bond length in 4^{8d} is elongated to 2.84 Å. Reference back to the contour plot of π^* in Figure 5 shows that considerable electron density in TT^{2-} will be accumulated on the carbonyl ligands, as well as the two metal atoms. The replacement of CO by other auxillary ligands, e.g., phosphines, should cause especially the second reduction potential to increase and may even influence the stability of TT^{2-}. This is a topic which we shall pursue in the future.

Acknowledgment. We thank the Robert A. Welch Foundation and the National Science Foundation (CHE 82-11883) for generous support of this work, S. H. Kang for the drawings, and B. Cornelius for the typing.

Appendix

All calculations were performed with the extended Hückel method[11] using the modified Wolfsberg–Helmholz formula.[17] The H_{ii}'s and orbital exponents listed in Table I were taken from previous work.[7] All Rh–C, C–O, and P–H distances were set at 1.87, 1.14, and 1.41 Å, respectively. The C–Rh–C angles at the square-planar and tetrahedral geometries were fixed at 90.0° and 111.6°, respectively. A uniform variation of the C–Rh–C angle was assumed for intermediate geometries. The H–P–H angles were set at 106.0°.

Registry No. $Rh_2(CO)_4(PH_2)_2$, 94904-44-6.

(17) Ammeter, J. H.; Bürgi, H. B.; Thibeault, J. C.; Hoffmann, R. *J. Am. Chem. Soc.* **1978**, *100*, 3686.

A Theoretical Study on the Proton Affinity of Some Mononuclear d^8 and d^{10} Metal Carbonyls by the Hartree–Fock–Slater Transition-State Method

Tom Ziegler

Department of Chemistry, University of Calgary, Calgary, Alberta, Canada T2N 1N4

Received September 5, 1984

Hartree–Fock–Slater calculations are reported on the protonation energies for the d^8 pentacarbonyls $M(CO)_5$ (M = Fe, Ru, Os), $M(CO)_5^-$ (M = Mn, Tc, Re), $Cr(CO)_5^{2-}$, and $Co(CO)_5^+$ as well as the d^{10} tetracarbonyls $M(CO)_4^-$ (M = Co, Rh, Ir), $M(CO)_4$ (M = Ni, Pd, Pt), $Fe(CO)_4^{2-}$, and $Cu(CO)_4^+$. The calculated protonation energies were decomposed into electrostatic ($\Delta E°$), electronic (ΔE_{elec}), and relativistic (ΔE_R) contributions as well as contribution (ΔE_{prep}) from the rearrangement of the $M(CO)_5$ and $M(CO)_4$ frameworks on formation of the hydrides. The electronic term ΔE_{elec} was calculated to increase vertically down a triad and decrease along a transition series with increasing nuclear charge on the metal. A possible explanation for the calculated trends in ΔE_{elec} is given in terms of simple perturbational molecular orbital (PMO) theory, and it is suggested that the trends in ΔE_{elec} calculated for the electrophile H^+ apply to other electrophiles as well.

Introduction

The ability of a metal in a low-valent complex to act as a good nucleophile is of crucial importance in several key-step catalytic processes, and there has as a consequence been considerable interest[1] in a quantitative characterization of the nucleophilicity of such complexes as a function of the metal atom as well as the coligands.

Much of our knowledge on the trends in nucleophilicity with respect to different metal centers comes from experimental solution studies[2] on the Brønsted acidity of transition-metal hydrides or the protonation basicity of transition-metal complexes. Such experimental studies are in part hampered by the air sensitivity of some transition-metal hydrides as well as the difficulty in finding a common suitable solvent for a variety of different hydrides. It is in addition difficult to gauge the difference in nucleophilicity between various metal centers from protonation/deprotonation solution studies alone, since the acidity of a transition-metal hydride, HML_n, in solution

(1) (a) Vaska, L. *Acc. Chem. Res.* **1968**, *1*, 335. (b) Tolman, C. A. *Chem. Soc. Rev.* **1972**, *1*, 337.

(2) (a) Vidal, J. L.; Walker, W. E. *Inorg. Chem.* **1981**, *20*, 249. (b) King, R. B. *J. Am. Chem. Soc.* **1966**, *88*, 5121. (c) Walker, H. W.; Kresge, C. T.; Ford, P. C.; Pearson, R. G. *J. Am. Chem. Soc.* **1979**, *101*, 7428 and references therein.

0276-7333/85/2304-0675$01.50/0